Suppressing artifacts in the total focusing method using the directivity of laser ultrasound

Huabin He, Kaihua Sun [*], Chaoming Sun, Jianguo He, Enfu Liang, Qian Liu

Institute of Machinery Manufacturing Technology, China Academy of Engineering Physics, Mianyang, Sichuan 621900, PR China

ARTICLE INFO

ABSTRACT

Based on a synthesized laser ultrasonic array, full matrix capture can be used to acquire data, which can then be post-processed using the total focusing method. However, this noncontact ultrasonic imaging technique has not been widely used because of the numerous artifacts in ultrasonic images and time-consuming data acquisition. To address these issues, this study proposes a post-processing algorithm, which uses the laser ultrasound directivity information to suppress the artifacts in the total focusing method's images. In particular, a weight factor is defined using the directivity information. By multiplying the image intensity of the total focusing method with this factor, the algorithm uses not only the amplitude and phase information of laser ultrasound but also its directivity information. The experimental results indicate that four types of artifacts are suppressed. Because the grating lobe artifacts can be suppressed, a larger element spacing can be used to reduce the data acquisition time.

1. Introduction

Ultrasonic imaging is intuitive and innocuous, making it one of the most widely used nondestructive evaluation (NDE) techniques [1]. In the past few decades, there has been a transition from NDE to quantitative NDE to help optimize the manufacturing process or improve structural health management [2]. Quantitative NDE refers to the measurement of each defect's size, shape, and location, which are then used to determine whether the defect will cause component failure. For this purpose, ultrasonic imaging techniques have been progressively developed to provide better image quality, such as fewer artifacts and less noise. An ultrasonic phased array provides better image quality than a single-element transducer and can almost meet the needs of quantitative NDE. However, the use of couplant makes ultrasonic phased arrays inapplicable to many scenarios, such as hazardous environments, fast-moving components, and high-temperature applications.

Compared with piezoelectric transducers, laser ultrasonics is couplant-free because lasers are used to generate and detect ultrasound [3–5]. Therefore, laser ultrasonics is a noncontact technique, which applies to those scenarios [6,7], can remotely inspect places with limited access, and can rapidly inspect complex-shaped components [8]. However, for nondestructive inspection, the component's ablation threshold limits the energy of the generation laser; therefore, the laser ultrasonic signals are weaker than those from the piezoelectric transducers.

Moreover, the detection sensitivity of optical methods, such as laser vibrometers, is lower than that of piezoelectric transducers; therefore, the signal-to-noise ratio (SNR) of laser ultrasonic signals is lower than that of piezoelectric transducers. When using laser ultrasonic C-scanning, the image quality suffers from weak signals and poor SNR.

Laser ultrasonic arrays (LUA) have been proposed to enhance laser ultrasonic images [9]. This can be achieved through spatial or temporal modifications of laser beams, but these systems are complex and expensive [10]. To reduce the complexity and expense, Stratoudaki et al. [10] synthesized an LUA by alternatively scanning a single-generation laser and a single-detection laser. To further increase the detection sensitivity of small defects, data were acquired using full matrix capture (FMC), and post-processed using an adapted total focusing method (TFM) [10–12]. With simplified hardware and good imaging quality, synthesized LUAs using FMC and TFM or adapted TFM have been applied to additively manufactured [13–15] and complex-shaped components [16].

However, ultrasonic images in these applications still contain considerable noise and artifacts [17]. This could be because a pulsed laser can simultaneously generate several modes of acoustic waves, such as shear, longitudinal, and surface waves, which interfere with one another in the TFM algorithm to produce artifacts [16]. On the other hand, to avoid grating lobe artifacts, the element spacing of the generation and detection cannot exceed half the ultrasonic wavelength [10].
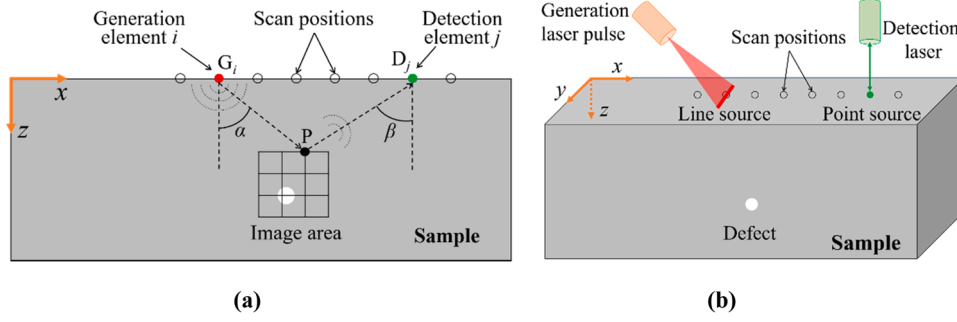

Fig. 1. Schematic diagram of a synthesized LUA: (a) the front view of the sample and (b) the oblique view of the sample.

Additionally, FMC data are acquired by serially collecting A-scan signals. Therefore, data acquisition in these applications is time-consuming. To accelerate FMC, Lukacs et al. [18] suggested a two-stage procedure. However, small defects might be omitted in the first stage when a large element spacing is used, and the element spacing is still limited by half the ultrasonic wavelength.

The aim of this paper is to suppress the artifacts in laser ultrasonic TFM images and reduce the data acquisition time. Therefore, we propose a post-processing algorithm that uses the directivity information of laser ultrasound to suppress artifacts in the TFM images. First, the correlation coefficient between the experimental and theoretical aperture data was computed to extract the directivity information included in the experimental aperture data. Then, a weight factor was defined using the correlation coefficient. Finally, the TFM image intensity was weighted using this factor. Section 2 introduces the directivity of laser ultrasound, principles of two existing and the proposed algorithms. Section 3 describes the samples and setup used in the experiments. In Section 4, results from the three algorithms are compared, and the causes of artifacts that the proposed algorithm suppresses are discussed. Finally, the conclusions are presented in Section 5.

2. Methods

A post-processing algorithm is proposed based on the TFM and laser ultrasound directivity information. Hence, the directivity of laser ultrasound and the principle of the TFM are introduced in the subsequent subsections. To compare the experimental results in Section 4, the principle of an adapted TFM presented in previous literature is introduced below.

2.1. Directivity of laser ultrasound

Laser ultrasound consists of three procedures. First, the optical energy is absorbed by the material surface and then converted into heat. Second, heat produces rapid thermal expansion and stress. Finally, while the pulsed laser attenuates and heat is transmitted to other regions of the material, the thermal expansion decreases to produce vibrational displacement, namely, ultrasound [19]. The temporal characteristics of the laser pulse determine the ultrasound's broadband bandwidth [20, 21]. In the thermoelastic regime, the power density of the laser pulse is lower than the ablation threshold of the material, so the whole process is nondestructive. In this regime, for aluminum, the radiated energy of shear waves is approximately ten times that of longitudinal waves [22]. Therefore, shear waves were used in this study.

The generation directivity of laser ultrasound implies that the wave amplitude generated using a laser pulse varies with the observation angle. In the thermoelastic regime, the generation directivity of shear waves is expressed as follows [23,24]:

$$g(\alpha) \propto \frac{\sin 2\alpha \cos 2\alpha}{\cos^2 2\alpha + 2 \sin \alpha \sin 2\alpha (\kappa^{-2} - \sin^2 \alpha)^{1/2}} \tag{1}$$

where α is the observation angle of the shear waves with respect to the surface normal, as shown in Fig. 1(a), $\kappa = c_L/c_T$ where c_L and c_T are the acoustic velocities of the longitudinal and shear waves, respectively.

The detection directivity of laser ultrasound implies that the signal amplitude detected by a laser vibrometer varies with the incident angle of ultrasonic waves because the vibrometer is only sensitive to the out-of-plane ultrasonic component. The detection directivity of the shear waves is expressed as follows [25]:

$$d(\beta) \propto \frac{\sin 2\beta (\kappa^2 \sin^2 \beta - 1)^{1/2}}{\kappa (2 \sin^2 \beta - 1)^2 - 4 \sin^2 \beta (\kappa^2 \sin^2 \beta - 1)^{1/2} (\sin^2 \beta - 1)^{1/2}} \tag{2}$$

where β is the incident angle of the shear waves with respect to the surface normal, as shown in Fig. 1(a).

2.2. Principles of TFM and normalized TFM

This subsection introduces the principles of two existing post-processing algorithms: TFM and normalized TFM. These algorithms are used to process the laser ultrasonic FMC data, which can be acquired using a synthesized LUA, as shown in Fig. 1(b).

The TFM is a typical delay-and-sum imaging algorithm. First, the image area is discretized into a grid, as shown in Fig. 1(a). Any point in the grid represents a pixel in the TFM image. Then, all A-scan signals in the FMC data are delayed and summed to focus on every pixel point. Given a pixel point P(x,z), the image intensity at this pixel is expressed as follows [16,26]:

$$I(x,z) = \left| \sum_{i=1}^{n} \sum_{j=1}^{m} h_{ij} \left(\left(|G_i P| + |D_j P| \right) / c_T \right) \right| \tag{3}$$

where $I(x,z)$ is the TFM image's intensity at the pixel point P(x,z); i and j are the sequence number of generation and detection elements, respectively; n and m are the total number of generation and detection elements, respectively; $|G_i P|$ is the distance between the generation point G_i and the pixel point P(x,z), as shown in Fig. 1(a); $|D_j P|$ is the distance between the detection point D_j and the pixel point P(x, z); $(|G_i P| + |D_j P|)/c_T$ represents the time-of-flight (TOF) of the shear waves; h_{ij} is the Hilbert transform of an A-scan signal. Using the Hilbert transform, a coherent sum is realized to use the phase information of laser ultrasound. Before the Hilbert transform, the A-scan signal should be digitally filtered to increase the SNR.

The normalized TFM was adapted from the TFM [11]. Apodization coefficients were introduced to further increase the SNR of TFM images while considering the directivity of generation and detection. In particular, in the TFM's summation procedure, the contribution of each A-scan signal is weighted using the apodization coefficient. As a result, the revised TFM image has uniform noise but non-uniform sensitivity [10]. To normalize the sensitivity of the revised TFM image, it is divided by a sensitivity image, as follows [11]:
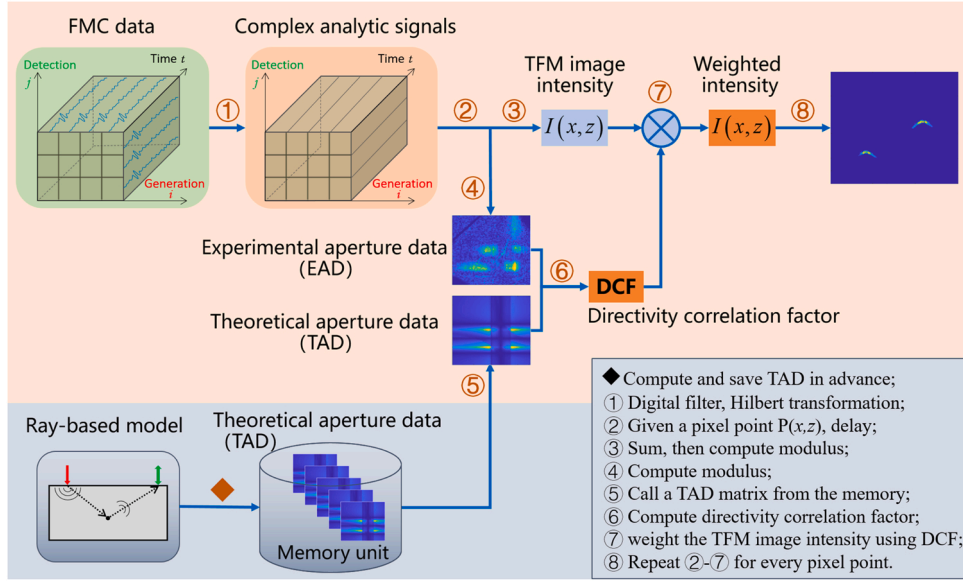
Fig. 2. Overview of the proposed algorithm: weighted TFM using the directivity correlation factor.

$$I_n(x,z) = \frac{I_{revised}(x,z)}{I_{sensitivity}(x,z)}$$

$$= \frac{\left| \sum_{i=1}^{n} \sum_{j=1}^{m} \left(\frac{g(\alpha_i)}{|G_iP|^{1/2}} \frac{d(\beta_j)}{|D_jP|^{1/2}} h_{ij} \left(\frac{|G_iP| + |D_jP|}{c_T} \right) \right) \right|}{\left| \sum_{i=1}^{n} \sum_{j=1}^{m} \left(\frac{g(\alpha_i)}{|G_iP|^{1/2}} \frac{d(\beta_j)}{|D_jP|^{1/2}} \right)^2 \right|} \quad (4)$$

where $I_n(x,z)$ is the intensity of the normalized TFM image; $I_{revisd}(x,z)$ is the intensity of the revised TFM image; $I_{sensitivity}(x,z)$ is the intensity of the sensitivity image; $\frac{g(\alpha_i)}{|G_iP|^{1/2}}$ and $\frac{d(\beta_j)}{|D_jP|^{1/2}}$ are the apodization coefficients.

Because the normalized TFM considers the directivity information using apodization coefficients, it can suppress some artifacts in the TFM images. However, this suppression is limited because of the drawbacks of the weighted summation in the numerator of Eq. (4), which will be analyzed in detail in Section 4.

2.3. Weighted TFM using directivity correlation factor

This section proposes a post-processing algorithm to achieve better image quality. Fig. 2 shows an overview of the proposed algorithm.

The TFM algorithm has two main procedures: delay and sum, as shown in Eq. (3). Given a pixel point P(x,z), after the time delay, a data set is acquired by computing the modulus:

$$H_{ij} = \left| h_{ij} \left(\left(|G_iP| + |D_jP| \right) / c_T \right) \right| \quad (5)$$

where $i = 1, 2, \cdots, n$ and $j = 1, 2, \cdots, m$. This data set can also be expressed as a matrix, called the experimental aperture data (EAD):

$$\mathbf{H} = \begin{bmatrix} H_{11} & \cdots & H_{1m} \\ \vdots & \ddots & \vdots \\ H_{n1} & \cdots & H_{nm} \end{bmatrix} \quad (6)$$

where $\mathbf{H}$ has $n \times m$ dimensions. The EADs and pixel points have a one-to-one correspondence. We observed that an EAD contains not only the amplitude information of the laser ultrasound but also directivity information, which may be revealed from its image pattern. If an algorithm can distinguish between the image patterns of EADs at defect points and those at intact points, the algorithm may enhance defects and have fewer artifacts.

To determine this distinction, a ray-based forward model [10] was used to simulate the LUA's response to a small target. If the generation and detection points are in the target's far field and the target is a perfect point target (that is, the scattering matrix is equal to unity), the response can be expressed as follows:

$$F_{ij} = \left| \frac{g(\alpha_i)}{|G_iP|^{1/2}} \frac{d(\beta_j)}{|D_jP|^{1/2}} \right| \quad (7)$$

where $i = 1, 2, \cdots, n$ and $j = 1, 2, \cdots, m$. The response can also be expressed as a matrix, called the theoretical aperture data (TAD), as follows:

$$\mathbf{F} = \begin{bmatrix} F_{11} & \cdots & F_{1m} \\ \vdots & \ddots & \vdots \\ F_{n1} & \cdots & F_{nm} \end{bmatrix} \quad (8)$$

where $\mathbf{F}$ and $\mathbf{H}$ have the same dimension. Additionally, the TADs and target positions have a one-to-one correspondence. The values of F_{ij} are proportional, so they contain no amplitude information of laser ultrasound. However, the proportion between them, or the TAD image pattern, contains the directivity information of laser ultrasound.

The more similar an EAD is to the corresponding TAD, the more likely that the corresponding pixel point is a perfect point target, namely a defect. The similarity between the matrices $\mathbf{H}$ and $\mathbf{F}$ can be measured using their correlation coefficient, as follows:

$$Corr(\mathbf{H}, \mathbf{F}) = \frac{\sum_{i=1}^{n} \sum_{j=1}^{m} \left(H_{ij} - \overline{\mathbf{H}} \right) \left(F_{ij} - \overline{\mathbf{F}} \right)}{\sqrt{\left(\sum_{i=1}^{n} \sum_{j=1}^{m} \left(H_{ij} - \overline{\mathbf{H}} \right)^2 \right) \left(\sum_{i=1}^{n} \sum_{j=1}^{m} \left(F_{ij} - \overline{\mathbf{F}} \right)^2 \right)}} \quad (9)$$

where $\overline{\mathbf{H}} = \left(\sum_{i=1}^{n} \sum_{j=1}^{m} H_{ij} \right) / (n \times m)$, $\overline{\mathbf{F}} = \left(\sum_{i=1}^{n} \sum_{j=1}^{m} F_{ij} \right) / (n \times m)$, and $Corr(\mathbf{H}, \mathbf{F})$ ranges from -1 to 1. When $-1 \leq Corr(\mathbf{H}, \mathbf{F}) \leq 0$, $\mathbf{H}$ does not correlate with $\mathbf{F}$, and the corresponding pixel point is almost impossible to be a defect. Using $Corr(\mathbf{H}, \mathbf{F})$, the directivity correlation factor (DCF) is defined as follows:

$$\mathrm{DCF}(x,z) = \max\{\varepsilon, Corr(\mathbf{H}, \mathbf{F})\} \quad (10)$$

where $0 \leq \varepsilon < 1$; max{,} selects the maximum value of the arguments to guarantee $0 \leq \mathrm{DCF}(x,z) \leq 1$.

The DCF primarily uses the directivity information of laser ultrasound and can be used to weight the TFM image's intensity, which mainly uses the amplitude and phase information. The weighted
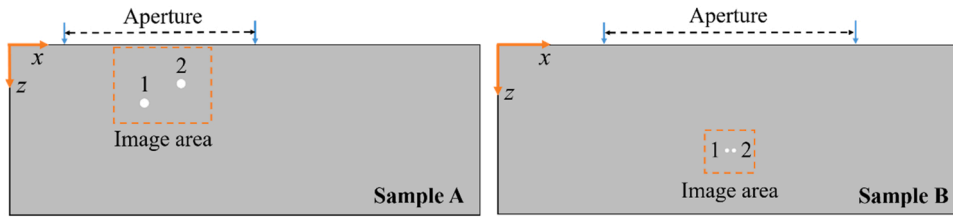
Fig. 3. Schematic diagram of samples A and B: front view.

Table 1
Characteristics of the samples.

Sample	Dimensions (mm)	Density (kg/m³)	Acoustic velocities (m/s)
A B	$x \times y \times z$: 100 × 40 × 40	$\rho = 2700$	Shear wave: $c_T = 3116.4$ Longitudinal wave: $c_L = 6367$ Surface wave: $c_R = 2910$

Table 2
Characteristics of the defects.

Sample	Defect	Center position (mm)	Diameter (mm)
A	1	$x = 30, z = 15$	2
	2	$x = 38, z = 10$	2
B	1	$x = 49.5, z = 25$	0.5
	2	$x = 50.5, z = 25$	0.5

intensity can be expressed as follows:

$$I_{weighted}(x, z) = (\mathrm{DCF}(x, z))^p \left| \sum_{i=1}^{n} \sum_{j=1}^{m} h_{ij}\big(\big(|G_iP| + |D_jP|\big)/c_T\big) \right| \quad (11)$$

where the power exponent p is used to adjust the sensitivity, and $I_{weighted}(x, z)$ is the image intensity of the proposed algorithm, named the weighted TFM. In this algorithm, TADs can be computed, saved in advance, and used repeatedly; therefore, they have no impact on post-processing time. Hence, the weighted TFM has the same algorithm complexity as the TFM and the normalized TFM.

Contrary to the weighted summation in the normalized TFM, the correlation coefficient is only sensitive to the global pattern of EADs and can suppress the effects of local interference in EADs. Therefore, the weighted TFM may contain fewer artifacts than the normalized TFM. To verify this hypothesis, experiments were performed as described below.

3. Experiments

3.1. Samples

Two aluminum samples, referred to as samples A and B, were used in this study, as shown in Fig. 3. The samples' upper surfaces were polished to a roughness of Ra 0.4 μm to increase the amount of light reflected to the interferometer. Each sample contained two through-hole defects. The characteristics of the samples and defects are listed in Tables 1 and 2, respectively.

3.2. Experimental setup

The experimental setup consisted of three systems: generation, detection, and scanning and acquisition, as shown in Fig. 4.

The generation laser was an Nd: YAG pulsed laser with a repetition rate of 1 kHz, a pulse duration of 10 ns, and a pulse energy of 1 mJ. Ultrasonic waves were generated in the thermoelastic regime. The laser beam was split into two beams using a beam splitter. One beam was detected using a photoelectrical detector to trigger a digital oscilloscope. The other beam was focused onto a line source along the y-axis using a cylindrical lens. A line source has a larger area than a point source, can reduce energy density, and can enhance generation directivity [10]. The other characteristics of the generation laser are listed in Table 3.

The detection laser was emitted from an interferometer and focused

Table 3
Characteristics of the generation and detection lasers.

Laser	Wavelength (nm)	Source shape	Source Dimensions (mm)	Incident angle
Generation	1064	Line source	$x \times y$: 0.2 × 3	45°
Detection	532	Point source	Diameter: 0.1	0°

I. Generation
1. Generation laser;
2. Plane mirror;
3. Beam splitter;
4. Cylindrical lens;
5. Plane mirror;
6. Sample(front view);
II. Detection
7. Lens of the detection laser;
8. Interferometer;
III. Scanning and acquisition
9. Linear motor stage;
10. Linear motor stage;
11. Controller of the stages;
12. Photoelectrical detector;
13. Digital oscilloscope;
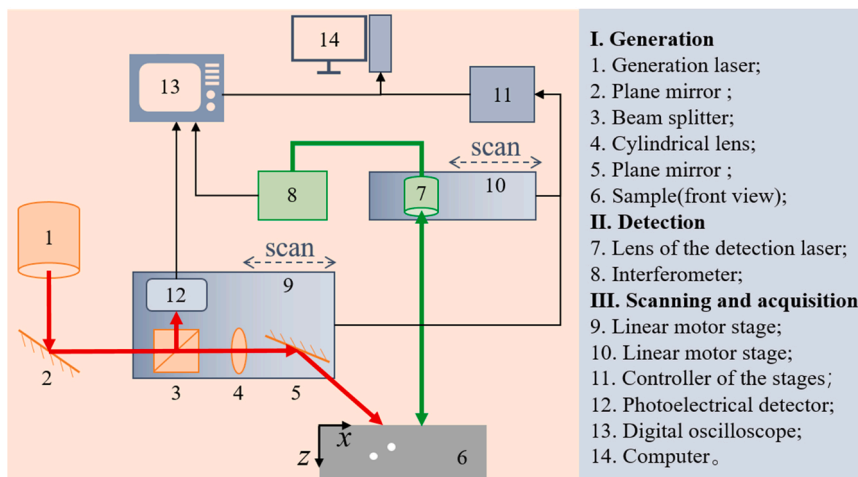14. Computer。

Fig. 4. Schematic diagram of the experimental setup.

Table 4
Parameters of scanning.

Sample	Aperture (mm)	Element spacing (mm)	Number of elements
A	$x \in [12,54]$	0.6	71
B	$x \in [24,76]$	0.5	105

Table 5
Parameters of imaging.

sample	Imaging area (mm)	Spacing of pixels (mm)	Image dimensions
A	$x \in [25,43]$, $z \in [1,19]$	0.1	181×181
B	$x \in [45.5, 54.5]$, $z \in [20.5, 29.5]$	0.05	181×181

down to a spot aligned to the center of the generation line source. The detection laser was a continuous wave laser with an average power of 500 mW and can continuously detect the out-of-plane displacement of the ultrasonic waves. Other characteristics of the detection laser are listed in Table 3.

An LUA was synthesized by alternately scanning the generation and detection lasers using two linear motor stages, with the sample remaining stationary. For each sample, the element positions of generation coincided with those of detection, and these positions are denoted in Table 4. Every time the two stages reached their predetermined positions, the computer instructed the digital oscilloscope to begin operating. When the trigger signal arrives, the oscilloscope samples the interferometer signal to obtain an A-scan signal. For each A-scan signal, the sampling time interval and number were 3.2 ns and 12,500, respectively. Hence, the FMC data of samples A and B had the dimensions of $71 \times 71 \times 12500$ and $105 \times 105 \times 12500$, respectively. Each A-scan signal was averaged 500 times to increase the SNR. Since
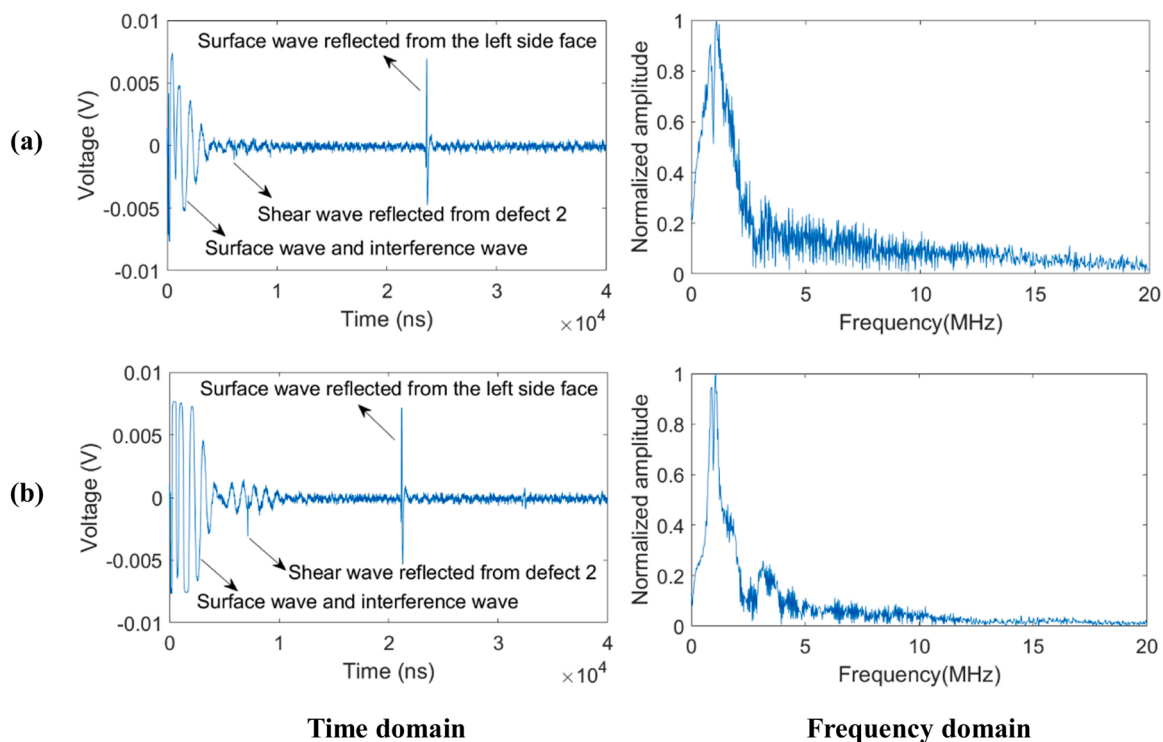
Fig. 5. Some of the original data of sample A before the digital filtering: (a) both the generation and detection points are located at x = 34.8 mm; (b) both the generation and detection points are located at x = 31.2 mm.
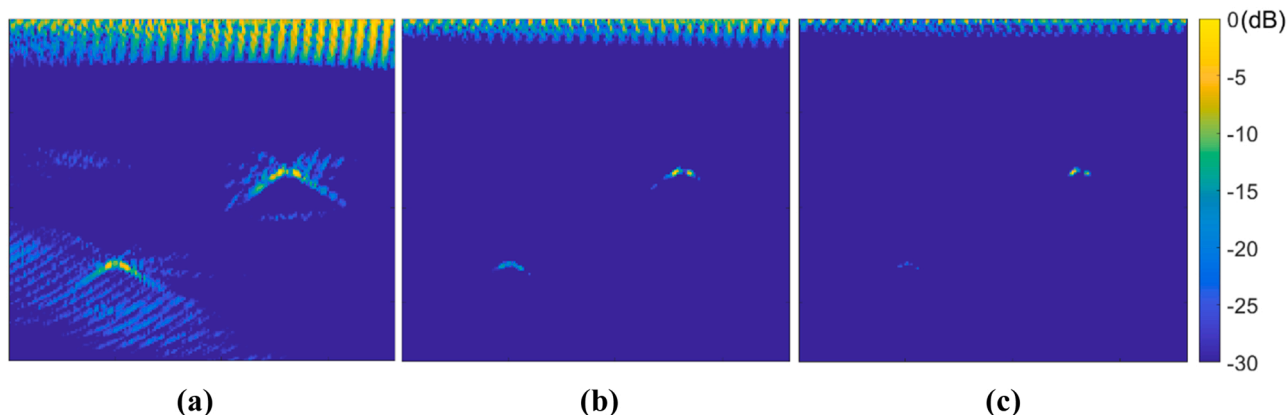
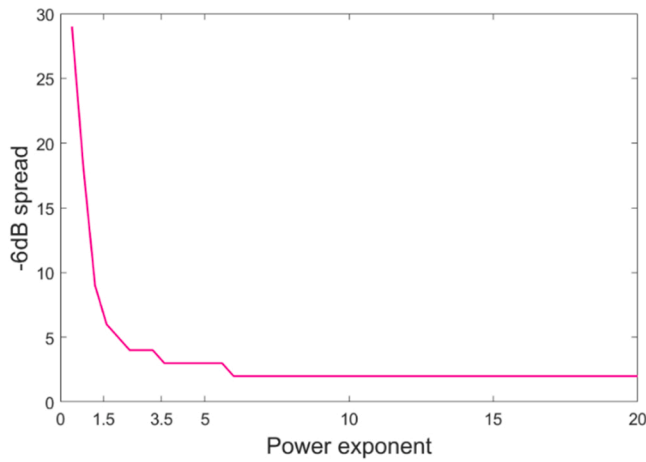**Fig. 6.** Weighted TFM images of sample A: (a) $p = 0.5$; (b) $p = 2.5$; (c) $p = 4.5$.

Fig. 7. -6 dB spread (weighted TFM images of sample A) varying as a function of the power exponent.

the repetition rate of the generation laser is 1 kHz, the time for data acquisition and averaging is approximately 0.5 s for each A-scan signal.

Fig. 3 shows the areas for imaging, and Table 5 lists the parameters. The pixel spacing of sample B needs to be smaller to obtain sufficient resolution because the defects in sample B are smaller than those in sample A.

4. Results and discussion

Fig. 5 shows some of the original data of sample A before the digital filtering. The interference wave is caused by the small distance between the generation and detection points. To evaluate the SNR, the maximum amplitude of the shear wave reflected from defect 2 was treated as the desired signal, which can be acquired by computing the shear wave's TOF. The root mean square of the signal amplitude from 2.56×10^4 ns to 4×10^4 ns was used to estimate the noise. The SNR of the signal shown in Fig. 5(a) is 14.49 dB, and the SNR of the signal shown in Fig. 5(b) is 23.21 dB.

A Gaussian digital filter with a central frequency and full width at half maximum (FWHM) of 7 MHz and 5 MHz, respectively, was used for post-processing. All the resulting images were logarithmically compressed and had the same dynamic range of 30 dB.

In the weighted TFM, the threshold ε determines the lower limit of DCF and further determines the dynamic range of the weighted TFM image. Therefore, ε should be small enough to acquire sufficient dynamic range. Additionally, it should be nonzero to avoid $-\infty$ in the logarithmically compressed image. In this study, ε was set to 1×10^{-5}.

To obtain the most appropriate value of the power exponent p, the weighted TFM images of sample A using different p were composed, and some of them are shown in Fig. 6. To quantify the image quality, these images' -6 dB spreads A_{-6dB} (focusing ability) were computed by counting the pixel points with intensity greater than -6 dB. The pixel points with depths less than 3 mm were not counted to exclude the surface wave artifacts. Fig. 7 shows the A_{-6dB} as a function of p. Fig. 6 and 7 show that when p is less than 1.5, A_{-6dB} decreases dramatically because the artifacts and noise in the images dramatically decrease. When p is greater than 3.5, A_{-6dB} decreases slowly, because the artifacts and noise tend to stabilize, and the defect profiles fade gradually. Therefore, the highest-quality image can be obtained near the function's turning point ($1.5 \leq p \leq 3.5$). For sample A, p can take any value between 1.5 and 3.5 because the image quality changes little in this range. In this study, it was set to 2.5.

The FMC data were post-processed on a laptop (CPU @ 2.60 GHz, 64 GB RAM). For sample A, the computation times of TFM, normalized TFM, and weighted TFM are 51.4 s, 56.3 s, and 56.9 s, respectively. The weighted TFM's computation time is close to that of the normalized TFM and approximately 10% longer than that of the TFM.

Fig. 8 shows the results of sample A. The TFM and normalized TFM images have many artifacts, most of which are suppressed in the weighted TFM image. Fig. 9 shows how these artifacts are suppressed. In Fig. 9(a), a randomly chosen artifact point A in the TFM image is labeled, and its corresponding EAD and TAD are shown in Fig. 9(b) and (c), respectively. These two matrices are obviously not correlated. Their correlation coefficient is -0.086, computed using Eq. (9); hence, the DCF computed using Eq. (10) is 1×10^{-5}. Weighted using this small DCF, the intensity of this point sharply decreases from -3.96 dB (in the TFM image) to less than -30 dB (in the weighted TFM image).

In Fig. 9(d), a randomly chosen artifact point B in the normalized TFM image is labeled, and its corresponding EAD and TAD are shown in Fig. 9(e) and (f), respectively. A significant amount of intensity at the top left of this TAD and some interference at the top left of the EAD can be observed simultaneously. Through the weighted summation in the normalized TFM (Eq. (4)), this local interference causes the intensity of point B to be as large as -8.59 dB. Generally, during the weighted summation process, interference in the addends is suppressed when a small weight factor is encountered. However, it increases when a significant weight factor is encountered. Therefore, weighted summation has a limited ability to suppress interference in EADs. Conversely, the correlation coefficient in the weighted TFM (Eq. (9)) is only sensitive to the global patterns of EADs and can suppress local interference. Therefore, most artifacts in the normalized TFM image are suppressed in the weighted TFM image.

In Fig. 9(g), a defect point C in the weighted TFM image is labeled, and its corresponding EAD and TAD are shown in Fig. 9(h) and (i),
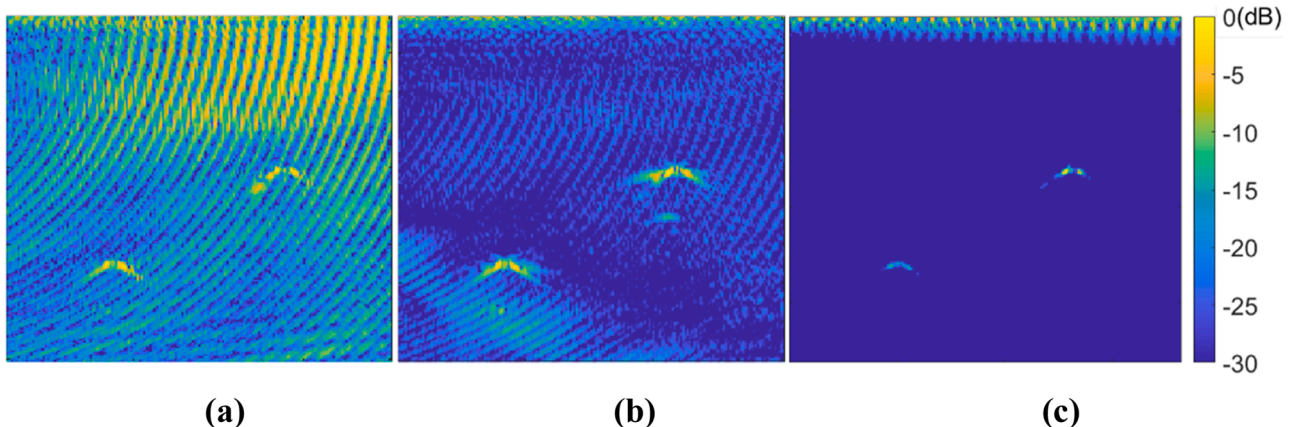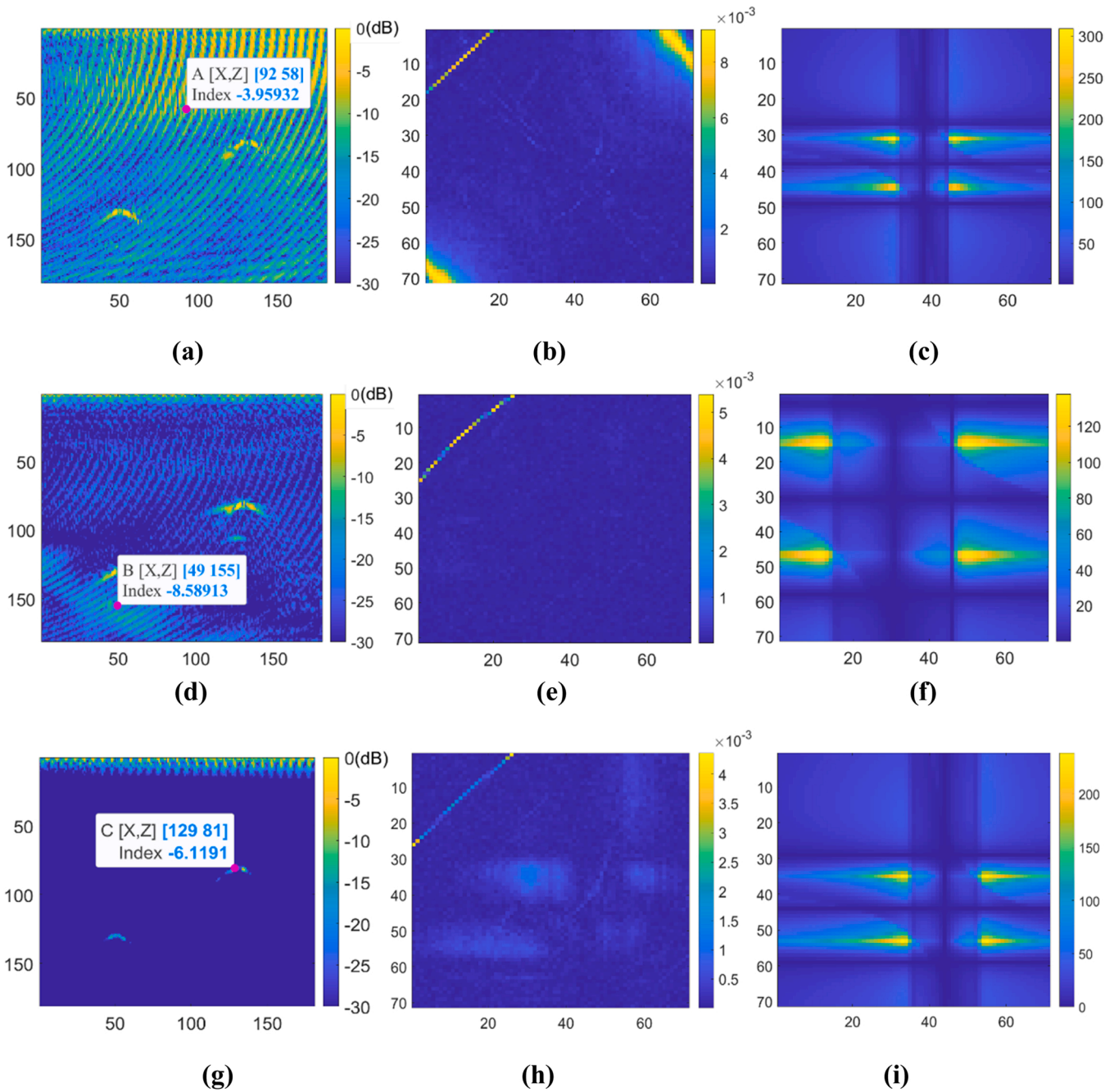

Fig. 8. Results of sample A: (a) TFM, (b) normalized TFM, and (c) weighted TFM.

Fig. 9. (a) TFM image with an artifact point A(92,58) labeled; (b) EAD of point A; (c) TAD of point A; (d) normalized TFM image with an artifact point B(49,155) labeled; (e) EAD of point B; (f) TAD of point B. (g) weighted TFM image with a defect point C(129,81) labeled; (h) EAD of point C; and (i) TAD of point C.

respectively. Despite the local interference at the top left of the EAD, the global patterns of these two matrices are similar, with a correlation coefficient of 0.43. This indicates that the directivity information from the experimental results (EAD) is consistent with the theoretical results (TAD) at defect points.

In the following subsections, the causes of these artifacts are analyzed and verified individually.

4.1. Suppressing artifacts caused by surface waves

In Figs. 8(a) and 8(b), the most severe artifacts are the arc stripes. Because they are asymmetrical, we assumed that they are related to the sample's side face, and that they are caused by the surface waves reflected from the left side face. To verify this hypothesis, we excluded

these surface waves from the FMC data [16] by setting the amplitude of each A-scan signal to 2.5×10^{-5} when $\left| t_{ij} - t_{ij}^{left} \right| = \triangle t$, where t_{ij}^{left} is the TOF of the surface wave from the generation element i to the left side face of the sample and then reflected to the detection element j, and $\triangle t$ is the pulse width, which is 1.28 μs in this study. The resulting images shown in Fig. 10(a) demonstrate that the arc-shaped artifacts were caused by the surface waves reflected from the left side face.

As shown in Fig. 10(a), there are still many artifacts in the upper half of the TFM and normalized TFM images, and there are also a few artifacts in the top of the weighted TFM image. Considering the artifacts' location, we assumed that they were caused by the surface waves that traveled directly from generation to detection. Similarly, these surface waves were excluded, and the results are shown in Fig. 10(b).
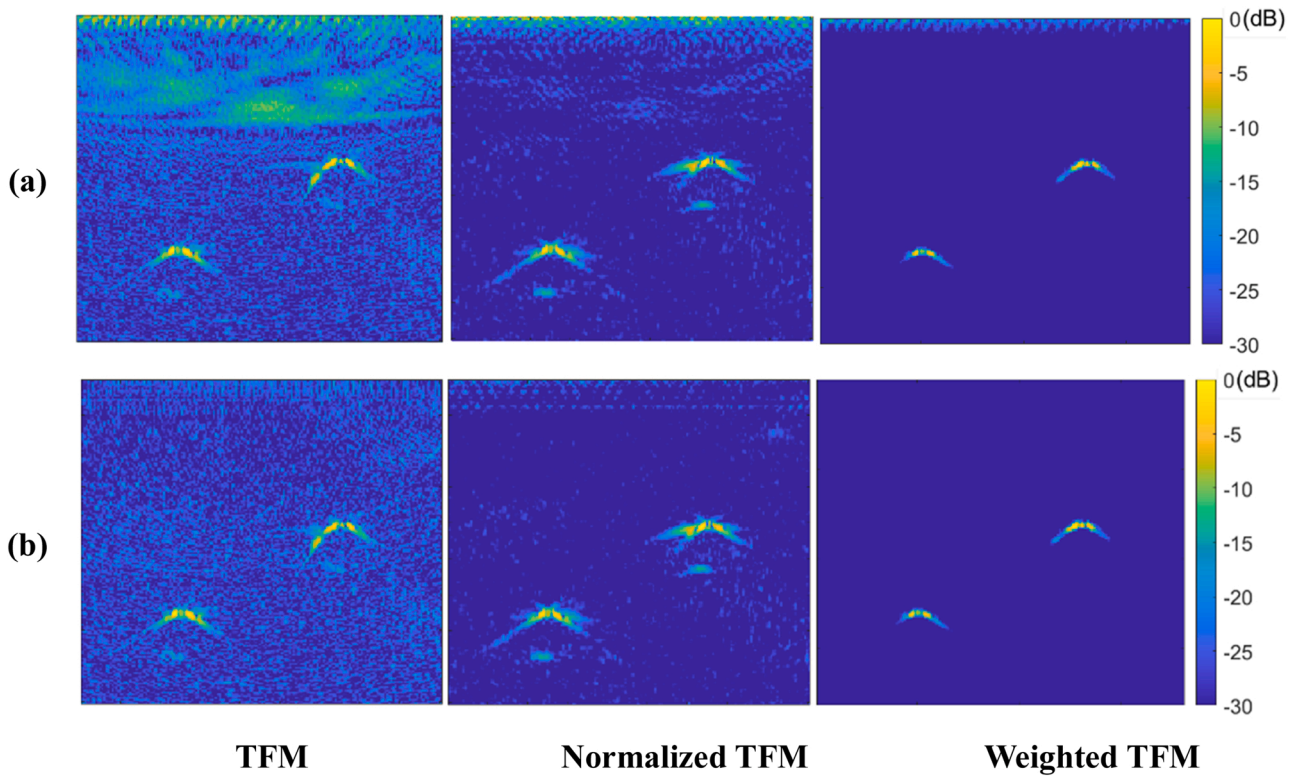
Fig. 10. Results of sample A: (a) the surface waves reflected from the sample's left side face were excluded from the FMC data and (b) the surface waves that travel directly and reflected from the sample's left side face were all excluded from the FMC data.
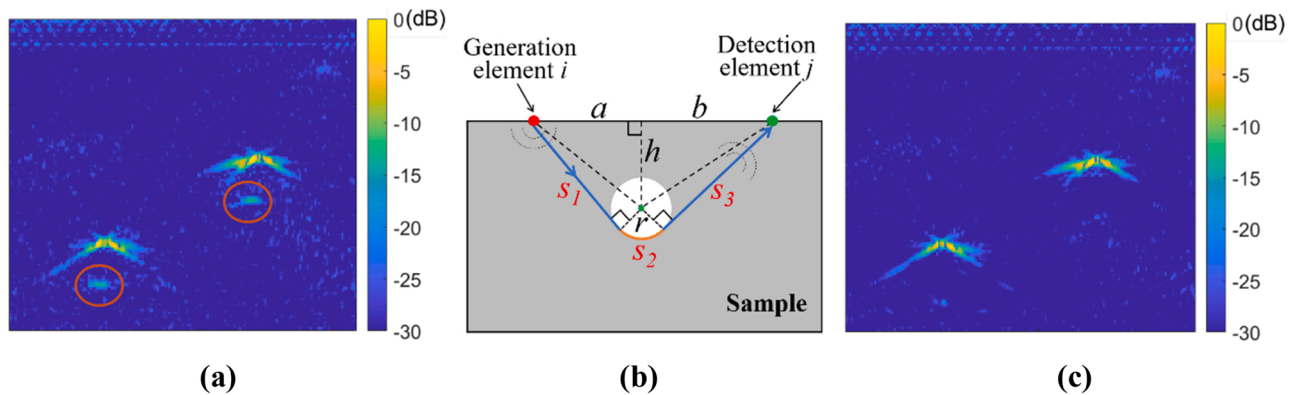
Fig. 11. (a) normalized TFM image with two artifact regions circled; (b) schematic diagram of the SCS waves scattered from the defect's bottom surface; and (c) normalized TFM image after the SCS waves were excluded from the FMC data.

By comparing Figs. 10 and 8, it can be concluded that the weighted TFM can suppress the artifacts caused by the surface waves that travel directly and reflected from the sample's side face. It should be noted that the artifacts with depths less than 3 mm are difficult to suppress using weighted TFM, because the ray-based model used in Eq. (7) has a constraint that the generation and detection points must be in the far field of the perfect point target.

4.2. Suppressing artifacts caused by creeping waves

In Fig. 11(a), two artifact regions are circled in the normalized TFM image. Because they were just below the two defects, we assumed that they were caused by shear-creeping-shear (SCS) mode-converted waves scattered from the defect's bottom surface [27].

To verify this hypothesis, we excluded these waves from the FMC data. As shown in Fig. 11(b), if the positions of the generation, detection,

and defect center are known, the distances a, b, and h can be calculated. If the defect radius r is known, the TOF of the SCS waves can be expressed as follows:

$$t_{CSC} = s_1/c_T + s_2/c_{Creep} + s_3/c_T \tag{12}$$

where

$$s_1 = \left((a^2 + h^2) - r^2\right)^{1/2}; \tag{13}$$

$$s_3 = \left((b^2 + h^2) - r^2\right)^{1/2}; \tag{14}$$

$$s_2 = r \times (2\pi - \arctan(a/h) - \arctan(b/h) - \arctan(s_1/r) - \arctan(s_3/r)); \tag{15}$$
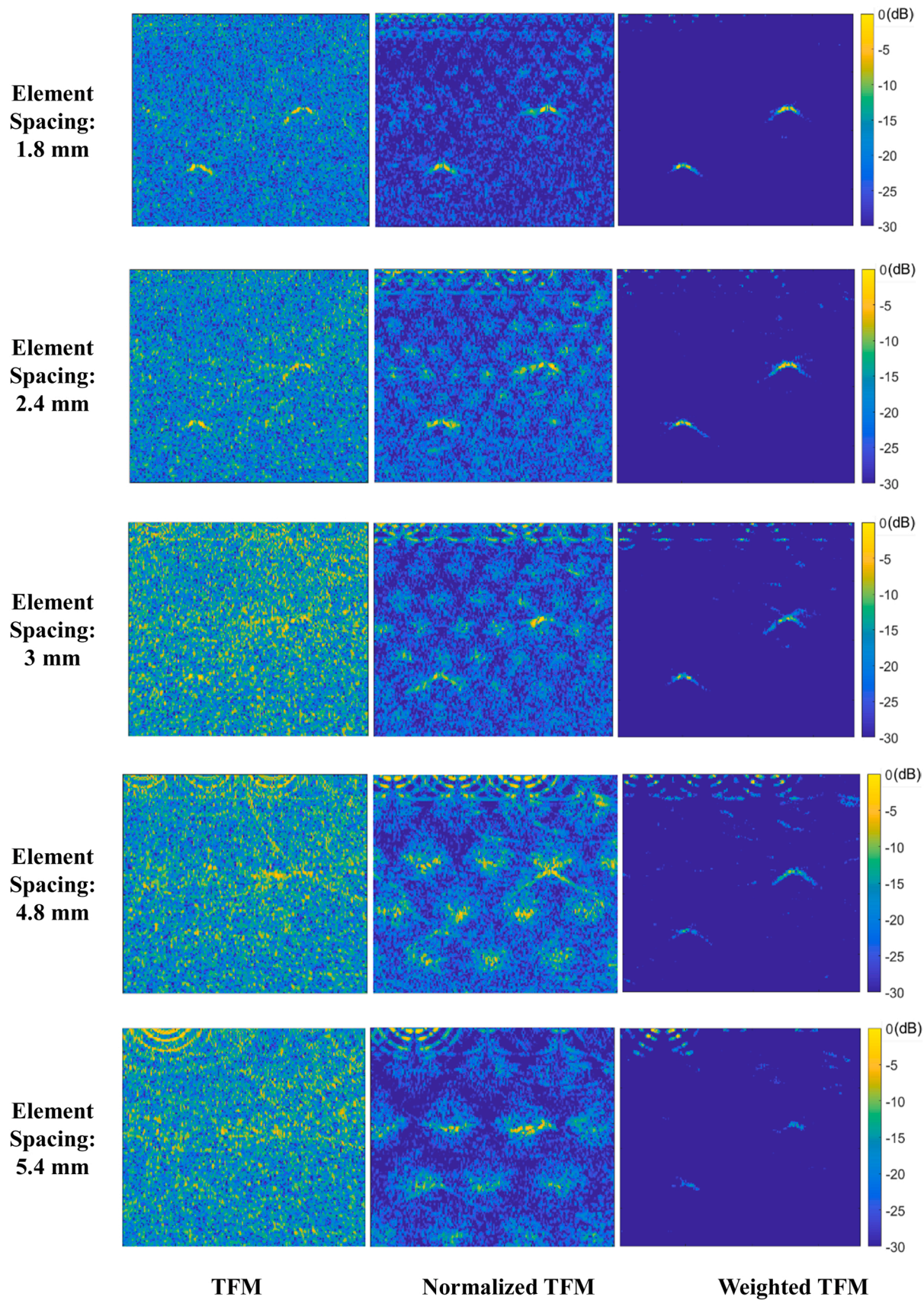
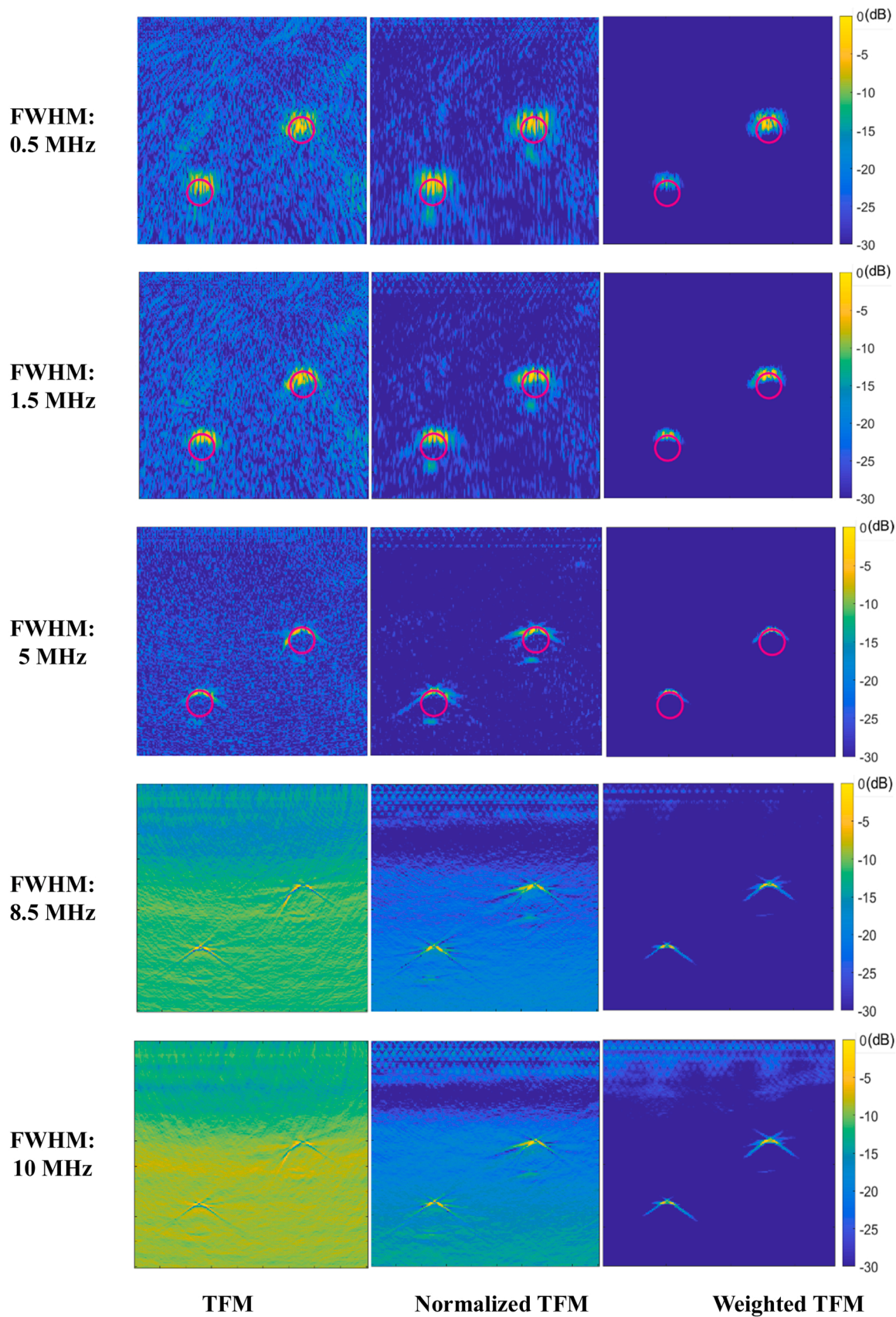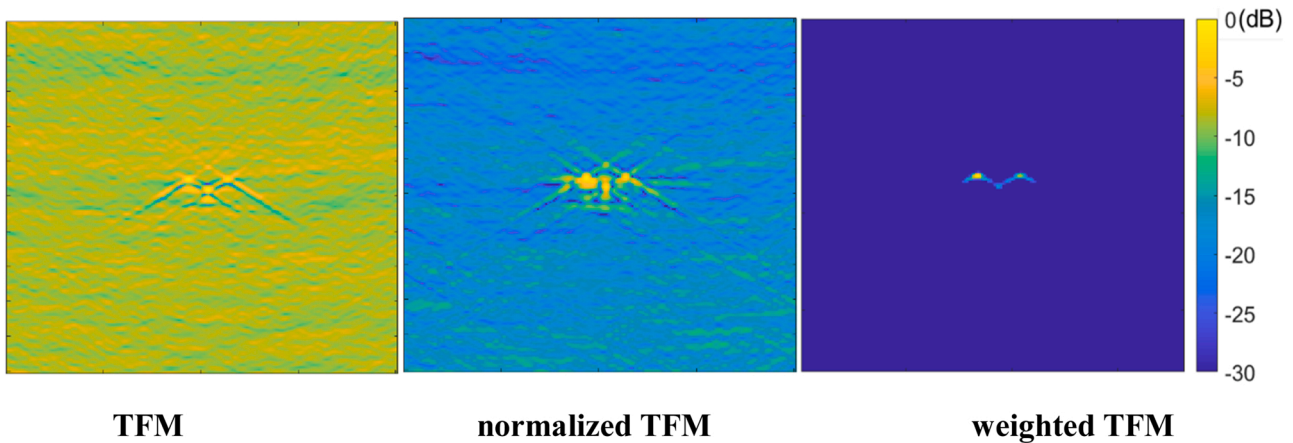**Fig. 12.** Results of sample A using subsets of the raw FMC data.

Fig. 13. Results of sample A using Gaussian filters with different FWHMs.

TFM   **normalized TFM**   **weighted TFM**

Fig. 14. Results of sample B with two defects, whose diameters are 0.5 mm, center distance is 1 mm, and depth is 25 mm.

$$c_{Creep} = c_T \Big/ \left(1 + 0.928(2\pi f_c r/c_T)^{-2/3}\right) \qquad (16)$$

where c_{Creep} is the acoustic velocity of creeping waves along arc lines [27] and f_c is the central frequency of the shear waves (7 MHz in this study).

The resulting image shown in Fig. 11(c) demonstrates that these artifacts were caused by the SCS waves. It should be noted that, during practical inspections, the position and radius of defects cannot be predicted, making it impossible to calculate the TOF; therefore, these artifacts cannot be removed by excluding the SCS waves from the FMC data. However, the weighted TFM can suppress these artifacts, as shown in Figs. 8 and 10.

4.3. Suppressing grating lobe artifacts and reducing data acquisition time

As shown in Fig. 10(b), after extracting the surface wave artifacts, there was a large amount of noise in the TFM image and grating lobe artifacts in the top of the normalized TFM image. The grating lobe artifacts and noise were suppressed in the weighted TFM image.

Grating lobe artifacts result from the element spacing being greater than half the ultrasonic wavelength [10]. In this study, the element spacing was 0.6 mm, and the wavelength was approximately 0.45 mm. Because the weighted TFM can suppress grating lobe artifacts, the element spacing may not be limited by half the ultrasonic wavelength. To verify this hypothesis, the element spacing was increased using subsets of the raw FMC data. For example, a sparse FMC dataset with an element spacing of 1.2 mm was obtained by deleting A-scan signals when i or j was an even number.

Finally, eight groups of sparse FMC data were obtained, and the element spacing for each group was 1.2 mm, 1.8 mm, 2.4 mm, 3 mm, 3.6 mm, 4.2 mm, 4.8 mm, and 5.4 mm. For brevity, five groups of images are displayed in Fig. 12. When the spacing is greater than 2.4 mm, the defect profiles can hardly be recognized in the TFM and normalized TFM images, but they can still be recognized in the weighted TFM image when the spacing is 4.8 mm. When the element spacing was 2.4 mm, the element number was 18, and there were 324 combinations of generation and detection. When the element spacing was 4.8 mm, there were only 81 combinations of generation and detection. Hence, the time required for data acquisition was reduced to approximately 25%.

In summary, the weighted TFM can suppress grating lobe artifacts and noise, so the element spacing can be increased to break through the limit of half wavelength and to reduce the data acquisition time.

4.4. Reducing the distortion of defect profiles

As shown in Fig. 10(b), the defect profiles are distorted in the TFM

and normalized TFM images. The defect profiles were divided into two or three fragments, each of which was distorted from an arc into a straight line. However, in the weighted TFM image, the defect profiles coincide with the actual profiles. It should be noted that only the upper profile of a defect can be imaged using shear waves reflected from the upper surface of the defect. The profiles in other directions can be imaged by scanning the laser in other directions or using other algorithms, such as multi-mode TFM [28].

When using a Gaussian filter, we found that the filter's FWHM is critical to the accuracy of the defect profiles. Fig. 13 shows the resulting images obtained using different FWHMs. The red circles indicate the actual defect profiles. The red circles were removed from the last six images to avoid sheltering the imaged profiles. As shown in Fig. 13, when the FWHM was greater than 5 MHz, the grating lobe artifacts and noise increased, and the artifacts around the defect profiles also increased. When it was less than 5 MHz, the thickness of the profiles increased to bury their real shapes. This is because, toward ultrasound propagation, the dimension of the defect indication in the resulting image is related to the ultrasonic pulse width and not to the actual defect size [2]. In this study, in the z-axis direction, the thickness of the defect profiles in the resulting images is related to the shear wave pulse width and not to the actual defect diameters.

Two adjacent small defects, having a diameter of 0.5 mm, a center distance of 1 mm, and a depth of 25 mm, in sample B were imaged to verify the performance of the weighted TFM further. The FWHM of the Gaussian filter was set to 6.5 MHz to preserve more of the high-frequency components. The power exponent p was decided in the same way of sample A and set to six. Fig. 14 illustrates that the weighted TFM can still accurately image the defect profiles with a higher SNR, better contrast, and better resolution even when the defect diameters are close to the ultrasonic wavelength.

5. Conclusions

A post-processing algorithm called weighted TFM was proposed to process FMC data acquired using a synthesized laser ultrasonic array. When the experimental results of this algorithm were compared with those of two existing algorithms, TFM and normalized TFM, weighted TFM was demonstrated to have several advantages. First, this algorithm can suppress artifacts caused by directly traveling surface waves, artifacts caused by the surface waves reflected from the side face of the sample, and artifacts caused by the shear-creeping-shear mode-converted waves scattered from the bottom surface of the defect. Second, this algorithm can suppress random noise and grating lobe artifacts; therefore, element spacing for generation and detection can be increased to break through the limit of half the ultrasonic wavelength and to reduce the data acquisition time. In this study, the time required was

reduced to approximately 25%. Finally, this algorithm can reduce the distortion of the defect profiles. When two small defects (diameter:0.5 mm, depth:25 mm) are located close to each other (center distance:1 mm), this algorithm can accurately image and distinguish their profiles. The synthesized laser ultrasonic arrays using FMC and weighted TFM have the potential to achieve noncontact quantitative NDE and obtain more industrial applications owing to improved image quality and less data acquisition time.

The weighted TFM was based on the laser ultrasonic directivity of the sample material. This algorithm is not applicable if the directivity cannot be calculated, as it would be for inhomogeneous materials, and it may not be able to produce high-quality images for coarse-grain materials where the directivity calculated using the theoretical model differs from that in the experimental results. In future studies, the applicability of this algorithm should be verified using more samples of different materials.

Declaration of Competing Interest

The authors declare that they have no known competing financial interests or personal relationships that could have appeared to influence the work reported in this paper.

Data Availability

Data will be made available on request.

Acknowledgment

References

[1] S. Zhang, E.Z. Zhang, P.C. Beard, A.E. Desjardins, R.J. Colchester, Dual-modality fibre optic probe for simultaneous ablation and ultrasound imaging, Commun. Eng. 1 (1) (2022) 20, https://doi.org/10.1038/s44172-022-00020-9.

[2] M.V. Felice, Z. Fan, Sizing of flaws using ultrasonic bulk wave testing: a review, Ultrasonics 88 (2018) 26–42, https://doi.org/10.1016/j.ultras.2018.03.003.

[3] I. Pelivanov, T. Buma, J. Xia, C.-W. Wei, M. O'Donnell, NDT of fiber-reinforced composites with a new fiber-optic pump–probe laser-ultrasound system, Photoacoustics 2 (2) (2014) 63–74, https://doi.org/10.1016/j.pacs.2014.01.001.

[4] P. Pyzik, A. Ziaja-Sujdak, J. Spytek, M. O'Donnell, I. Pelivanov, L. Ambrozinski, Detection of disbonds in adhesively bonded aluminum plates using laser-generated shear acoustic waves, Photoacoustics 21 (2021), 100226, https://doi.org/10.1016/j.pacs.2020.100226.

[5] C.-Y. Ni, C. Chen, K.-N. Ying, L.-N. Dai, L. Yuan, W.-W. Kan, Z.-H. Shen, Non-destructive laser-ultrasonic Synthetic Aperture Focusing Technique (SAFT) for 3D visualization of defects, Photoacoustics 22 (2021), 100248, https://doi.org/10.1016/j.pacs.2021.100248.

[6] K. Yi, P. Liu, S.-H. Park, H. Sohn, Femtosecond laser ultrasonic inspection of a moving object and its application to estimation of silicon wafer coating thickness, Opt. Lasers Eng. 148 (2022), 106778, https://doi.org/10.1016/j.optlaseng.2021.106778.

[7] H. Kim, K. Kim, N. Garcia, T. Fang, X. Jiang, Liquid metallic laser ultrasound transducer for high-temperature applications, Appl. Phys. Lett. 118 (18) (2021), 183502, https://doi.org/10.1063/5.0046052.

[8] V. James, D. Carswell, J. Riise, P.I. Nicholson, N. Graf, N. Huber, M. Gärtner, B. Reitinger, E. Scherleitner, P. Burgholzer, Robot deployed Laser-Ultrasonic NDT system for inspection of large aircraft structures. IOP Conference Series: Materials Science and Engineering, IOP Publishing, 2021, https://doi.org/10.1088/1757-899X/1024/1/012032.

[9] R. Lee, R.M. White, Excitation of surface elastic waves by transient surface heating, Appl. Phys. Lett. 12 (1) (1968) 12–14, https://doi.org/10.1063/1.1651832.

[10] T. Stratoudaki, M. Clark, P.D. Wilcox, Laser induced ultrasonic phased array using full matrix capture data acquisition and total focusing method, Opt. Express 24 (19) (2016) 21921–21938, https://doi.org/10.1364/OE.24.021921.

[11] T. Stratoudaki, M. Clark, P.D. Wilcox, Adapting the full matrix capture and the total focusing method to laser ultrasonics for remote non destructive testing. 2017 IEEE International Ultrasonics Symposium (IUS), IEEE, 2017, pp. 1–4, https://doi.org/10.1109/ULTSYM.2017.8092864.

[12] T. Stratoudaki, M. Clark, P.D. Wilcox, 2017. Full matrix capture and the total focusing imaging algorithm using laser induced ultrasonic phased arrays, AIP Conference Proceedings, AIP Publishing LLC, 2017, p. 020022. https://doi.org/10.1063/1.4974563.

[13] T. Stratoudaki, Y. Javadi, W. Kerr, P.D. Wilcox, D. Pieris, M. Clark, 2018. Laser induced phased arrays for remote ultrasonic imaging of additive manufactured components, 57th Annual Conference of the British Institute of Non-Destructive Testing, NDT 2018, 2018, pp. 174–182.

[14] D. Pieris, T. Stratoudaki, Y. Javadi, P. Lukacs, S. Catchpole-Smith, P.D. Wilcox, A. Clare, M. Clark, Laser Induced Phased Arrays (LIPA) to detect nested features in additively manufactured components, Mater. Des. 187 (2020), 108412, https://doi.org/10.1016/j.matdes.2019.108412.

[15] P. Lukacs, G. Davis, T. Stratoudaki, S. Williams, C.N. MacLeod, A. Gachagan, 2021. Remote ultrasonic imaging of a wire arc additive manufactured ti-6ai-4v component using laser induced phased array, 2021 IEEE International Instrumentation and Measurement Technology Conference (I2MTC), IEEE, 2021, pp. 1–6. https://doi.org/10.1109/I2MTC50364.2021.9459823.

[16] J. Chen, J. Xiao, D. Lisevych, Z. Fan, Laser-induced full-matrix ultrasonic imaging of complex-shaped objects, IEEE Trans. Ultrason., Ferroelectr., Freq. Control 66 (9) (2019) 1514–1520, https://doi.org/10.1109/TUFFC.2019.2924179.

[17] Y. Mei, J. Chen, Y. Zeng, L. Wu, Z. Fan, Laser ultrasonic imaging of complex defects with full-matrix capture and deep-learning extraction, Ultrasonics 129 (2023), 106915, https://doi.org/10.1016/j.ultras.2022.106915.

[18] P. Lukacs, T. Stratoudaki, P. Wilcox, M. Clark, A. Gachagan, Optimisation of data acquisition and processing for laser induced ultrasonic phased arrays. Proceedings of Meetings on Acoustics ICU, Acoustical Society of America, 2019, https://doi.org/10.1121/2.0001170.

[19] K. Zhang, Z. Zhou, Quantitative characterization of disbonds in multilayered bonded composites using laser ultrasonic guided waves, NDT E Int. 97 (2018) 42–50, https://doi.org/10.1016/j.ndteint.2018.03.006.

[20] C.B. Scruby, L.E. Drain, 2019. Laser ultrasonics: techniques and applications, Routledge 2019. https://doi.org/10.1201/9780203749098.

[21] S. Rajagopal, B.T. Cox, Modelling laser ultrasound waveforms: the effect of varying pulse duration and material properties, J. Acoust. Soc. Am. 149 (3) (2021) 2040–2054, https://doi.org/10.1121/10.0003558.

[22] L. Rose, Point-source representation for laser-generated ultrasound, J. Acoust. Soc. Am. 75 (3) (1984) 723–732, https://doi.org/10.1121/1.390583.

[23] M.-H. Noroy, D. Royer, M. Fink, Shear-wave focusing with a laser-ultrasound phased-array, IEEE Trans. Ultrason., Ferroelectr., Freq. Control 42 (6) (1995) 981–988, https://doi.org/10.1109/58.476540.

[24] J.R. Bernstein, J.B. Spicer, Line source representation for laser-generated ultrasound in aluminum, J. Acoust. Soc. Am. 107 (3) (2000) 1352–1357, https://doi.org/10.1121/1.428422.

[25] G. Miller, H. Pursey, The field and radiation impedance of mechanical radiators on the free surface of a semi-infinite isotropic solid, Proc. R. Soc. Lond. Ser. A. Math. Phys. Sci. 223 (1155) (1954) 521–541, https://doi.org/10.1098/rspa.1954.0134.

[26] C. Holmes, B.W. Drinkwater, P.D. Wilcox, Post-processing of the full matrix of ultrasonic transmit-receive array data for non-destructive evaluation, NDT e Int. 38 (8) (2005) 701–711, https://doi.org/10.1016/j.ndteint.2005.04.002.

[27] C. Pei, T. Fukuchi, H. Zhu, K. Koyama, K. Demachi, M. Uesaka, A study of internal defect testing with the laser-EMAT ultrasonic method, IEEE Trans. Ultrason., Ferroelectr., Freq. Control 59 (12) (2012) 2702–2708, https://doi.org/10.1109/TUFFC.2012.2511.

[28] J. Zhang, B.W. Drinkwater, P.D. Wilcox, A.J. Hunter, Defect detection using ultrasonic arrays: the multi-mode total focusing method, NDT e Int. 43 (2) (2010) 123–133, https://doi.org/10.1016/j.ndteint.2009.10.001.

Huabin He received his M.S. degree in Instrument Science and Technology from Beihang University in Beijing, China. He is currently pursuing the Ph.D. degree in Optical Engineering at China Academy of Engineering Physics. His current research interests include ultrasonic nondestructive testing, non-contact laser-ultrasound systems and ultrasonic imaging.

Kaihua Sun is an Associate Professor at Institute of Machinery Manufacturing Technology, China Academy of Engineering Physics. In 2014, he received Ph.D. from School of Science, Nanjing University of Science and Technology. His research directions are laser ultrasonic non-destructive testing technology and application, ultrasonic imaging, X-ray Digital Radiographic and Computer Tomography imaging.

Chaoming Sun is a Senior Engineer at Institute of Machinery Manufacturing Technology, China Academy of Engineering Physics. His research directions are resonant ultrasound spectroscopy and ultrasonic nondestructive testing.
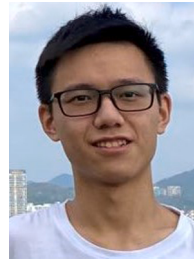
Enfu Liang received his bachelor's degree from Shanghai Jiao Tong University, and is currently pursuing the M.S. degree in Mechanical Engineering at China Academy of Engineering Physics. His current research interest includes ultrasonic resonance, vibrational nondestructive testing and SHM.

Jianguo He is a Senior Research Fellow and Ph.D. supervisor at Institute of Machinery Manufacturing Technology, China Academy of Engineering Physics. He is the deputy director of the Academic Committee of the Key Laboratory of Ultra-precision Machining Technology at China Academy of Engineering Physics. His most recent research has focused on advanced optical manufacturing and inspection technology.

Qian Liu is an Associate Professor at Institute of Machinery Manufacturing Technology (IMMT), China Academy of Engineering Physics (CAEP). He received his B.S. degree from Beijing Institute of Technology in 2006, and M.S., and Ph. D. degrees from CAEP in 2009 and 2015, respectively. His researching interests include interferometric and microscopic metrology, and optical sensor.